optica

Probing near-field light-matter interactions with single-molecule lifetime imaging: supplementary material

D. Bouchet, J. Scholler, G. Blanquer, Y. De Wilde, I. Izeddin*, and V. Krachmalnicoff*

Institut Langevin, ESPCI Paris, CNRS, PSL University, 1 rue Jussieu, 75005 Paris, France

**Corresponding authors: ignacio.izeddin@espci.fr, valentina.krachmalnicoff@espci.fr*

Published 25 January 2019

This document provides supplementary information to "Probing near-field light-matter interactions with single-molecule lifetime imaging," https://doi.org/10.1364/OPTICA.6.000135.

1. EXPERIMENTAL SETUP

A. Sample preparation

To prepare the sample, we spin-coat a dilute solution of silver nanowires in isopropyl alcohol on a glass coverslip. A microfluidic chamber is then prepared as follows [1]: we cover the sample with a ring made of parafilm, we place two micro-pipettes on opposite sides of the parafilm ring and we cover them with another glass coverslip before heating the sample up to 70°C in order to melt the parafilm. We let the microfluidic chamber cool down for a few minutes before using the micro-pipettes to inject biotin diluted in a phosphate-buffered saline (PBS) solution at a concentration of 1 g/L. We leave this solution incubate for 2 hours. Then, we inject streptavidin-conjugated fluorescent molecules (Alexa 647) diluted in a PBS solution at a concentration of 0.005 g/L, and we leave this new solution incubate for 2 hours. We add a PBS solution containing a few polystyrene fluorescent beads 100 nm in diameter (Red FluoSpheres, ThermoFisher Scientific) which we use as fiducial markers, and we then fill the chamber with an oxygen-reducing buffer [2]. This buffer is prepared according to the following protocol [3]: we use a PBS solution in which we dilute dextrose (100 mg/mL), cysteamine (3.86 mg/mL), glucose oxidase (0.5 mg/mL) and catalase (1.18 μL of an aqueous solution concentrated at 20-50 mg/mL).

B. Optical setup

Before the experiment, we select an area on the sample in which a silver nanowire can be identified by basic transmission imaging, thus ensuring that only one nanowire is present in the detection volume. Then, we place the area of interest in the middle of the field of view of the camera by using a piezoelectric stage (PXY 200SG, Piezosystem Jena). Photo-activatable molecules (Alexa Fluor 647) are excited by a pulsed laser diode emitting at $\lambda = 640$ nm (LDH Series P-C-640B, PicoQuant) at a repetition rate of 80 MHz. The intensity incident on the sample averaged over a repetition period is 10 μW/μm^2. The laser polarisation is set perpendicular to the nanowire axis in order to minimise the backscattering of the laser light by the nanowire. The molecules are photo-activated with a laser diode emitting at $\lambda = 405$ nm (LDH Series P-C-640B, Picoquant). During the acquisition, the density of activatable molecules decreases in time since several molecules are photobleached by the excitation laser. To compensate for this effect, we progressively turn on the photo-activation laser, with an average intensity on the sample up to 50 nW/μm^2. A third laser (Fianium SC450) filtered at $\lambda = 568$ nm is required for the excitation of fiducial markers that are used for real-time drift correction. These three lasers illuminate the sample through an oil immersion objective (UPLSAPO 100XO, NA=1.4, Olympus) mounted on an inverted microscope (Fig. S1). Wide-field illumination over an area of approximately 200 μm^2 is achieved by placing a lens ($f = 300$ mm) before the objective. Fluorescence from the sample is then collected by the objective and filtered by a dichroic mirror as well as two long-pass filters. Then, a 50:50 beamsplitter splits the signal towards two paths. On the first path, fluorescence photons are directed towards an EM-CCD camera (iXon 897, Andor). On the second path, a SPAD (PDM-R, Micro Photon Devices [4]) is connected to a time-correlated single-photon counting (TCSPC) system (HydraHarp400, Picoquant).

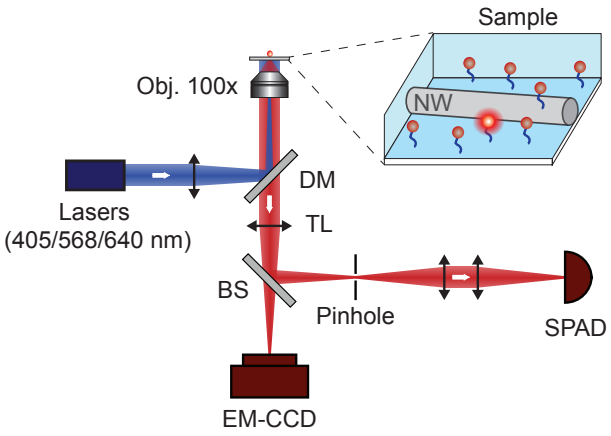

Fig. S1. Optical setup. The excitation laser ($\lambda = 640$ nm), together with the photo-activation laser ($\lambda = 405$ nm) and the laser used for sample stabilisation ($\lambda = 568$ nm), illuminate the sample via a high numerical aperture oil objective (NA=1.4). A lens (f=300 mm) is located on the excitation path to ensure wide-field illumination. Fluorescence from the sample is filtered with a dichroic mirror (DM) and passes through a tube lens (TL). A 50:50 beamsplitter (BS) splits the light towards an EM-CCD camera and a SPAD. The sample under study contains photo-activated single molecules in the near-field of a silver nanowire (NW).

C. Drift correction

To determine and correct the drift in the sample plane, we estimate the position of a fiducial marker from the wide-field images acquired by the camera and we use a feedback loop to maintain the marker at a fixed position. Every 5 s, the drift is estimated by fitting a two-dimensional Gaussian function to the image of the marker. A feedback signal is then applied on the piezoelectric stage (PXY 200SG, Piezosystem Jena) controlling the in-plane position of the sample in order to compensate for the drift.

In order to estimate the drift of the sample in the axial direction with respect to the focal plane, we analyse images of the fiducial marker accumulated over several seconds. The defocus-correction system is based on a real-time maximisation of the power spectral density of the measured images, and the axial position of the objective with respect to the sample is corrected in real time with a piezoelectric positioning system (MIPOS 20SG, Piezosystem Jena) located between the objective and the microscope turret.

2. POSITION AND DECAY RATE ASSOCIATION

A. Position estimations

The EM-CCD camera acquires 31 frames per second with an acquisition time of 30 ms per frame. The full sequence of wide-field images saved by the camera (over a subset of 13×13 pixels, pixel size = 160 nm) is imported by ImageJ [5] and the positions of the photo-activated molecules are estimated using ThunderSTORM [6]. First of all, each frame is filtered using a wavelet filter, as proposed by Izeddin *et al.* [7]. For each frame, approximate localisation of the molecules is then performed by applying a threshold that depends on the signal-to-noise ratio of the camera data. For this acquisition, we set it to 2.7 times the standard deviation of the intensity values obtained in the filtered image. Finally, sub-pixel localisation of the molecules is performed by fitting a two-dimensional Gaussian function to the data using the weighted least squares method on a restricted domain around the molecule (7×7 pixels). As some molecules can be identified over consecutive frames, we perform a merging of the data acquired by the camera if the estimated distance between successive detections is less than 40 nm. Then, the position of the molecule is determined by using the average value of the positions estimated from the different frames. Using this strategy, we obtain approximately 24,000 different detections for the whole experiment. This number is limited by the weak activation power required to ensure that no more than one molecule is typically active at a single time on the area conjugated to the SPAD.

B. Decay rate estimations

In addition to EM-CCD images, we also record the arrival time of each photon detected by the SPAD. To deal with the large size of the resulting file (∼15 GB), the 10-hour-long acquisition is split into several sequences of approximately 50 minutes. Then, we compute the number of detected photons as a function of time with a resolution of 500 μs. The intensity of background noise associated with this signal usually decreases during the experiment due to a decreasing number of activated molecules in the periphery of the detection area. Hence, the intensity time trace is Fourier filtered in order to remove low frequency components associated with temporal fluctuations longer than 30 s. Then, we consider that a molecule is potentially detected for each burst surpassing a given threshold that depends on the signal-to-noise ratio of the SPAD data. For each 50-minutes-long sequence, we set it to 2.6 times the standard deviation of the filtered signal. If another burst occurs within the typical blinking time scale (20 ms), it is attributed to the same molecule. In total, we identify approximately 14,000 events over the 10-hour-long acquisition. This value is small in comparison to the number of detections obtained from camera data. Indeed, the area of the sample conjugated to the SPAD (see Fig. S2b) is smaller than the area over which the localisation is performed ($\sim 1100 \times 1100$ nm). For each SPAD event, we build the associated decay histogram with a resolution of 16 ps in order to estimate the decay rate. To do so, the contribution of background noise is estimated by using close-by time intervals in which no burst can be identified. Then, the convolution of the instrument response function (IRF) and a decreasing mono-exponential function is fitted to the decay histogram using the least-squares method. The value of the decay rate is set to 10 ns^{-1} if the fit yields a value higher than this limit. Indeed, the IRF of the setup is characterised by a FWHM of approximately 240 ps (corresponding to 4 ns^{-1}) and we consider that estimates above 10 ns^{-1} are not meaningful even after the deconvolution process. While sample heterogeneities could induce multi-exponential decays, the small number of photons detected by the SPAD from each molecule does not allow to resolve different lifetimes. For this reason, we restrict the analysis to a mono-exponential decay, which would therefore correspond to an average over different decays.

C. Temporal and spatial correlations

It is important to keep in mind that the SPAD does not include information about the position of the molecules. We therefore need to ensure that the lifetime information provided by the SPAD is properly associated with the position of the molecules provided by the EM-CCD camera. At the beginning of the experiment, the acquisition of both camera and SPAD data is started by using an in-house software, and we can expect a time offset of several milliseconds between the two different channels. In order to precisely determine this time offset, we build two binary representations respectively associated with the SPAD events

and the camera detections (1 for a SPAD event or a camera detection, 0 otherwise). We then calculate the time correlation of these binary representations with a resolution of 500 μs, as shown in Fig. S2a for a typical sequence of 50 minutes. The maximum of this correlation coefficient gives an accurate estimate of the time offset between the camera and the SPAD. This delay is typically around 20 ms, which is consistent with the data acquisition procedure. Note that the correlation coefficient does not reach unity but is typically between 0.3 and 0.5. Indeed, the conditions required for the detection of a molecule by the camera and by the SPAD are different. In comparison to the SPAD, the camera is characterised by a larger field of view and a larger quantum efficiency. However, its lower temporal resolution makes the identification process less efficient for molecules characterised by fast temporal fluctuations. Hence we can expect some molecules to be detected by only one of the two detectors, resulting in a value smaller than unity for the maximum of the correlation coefficient.

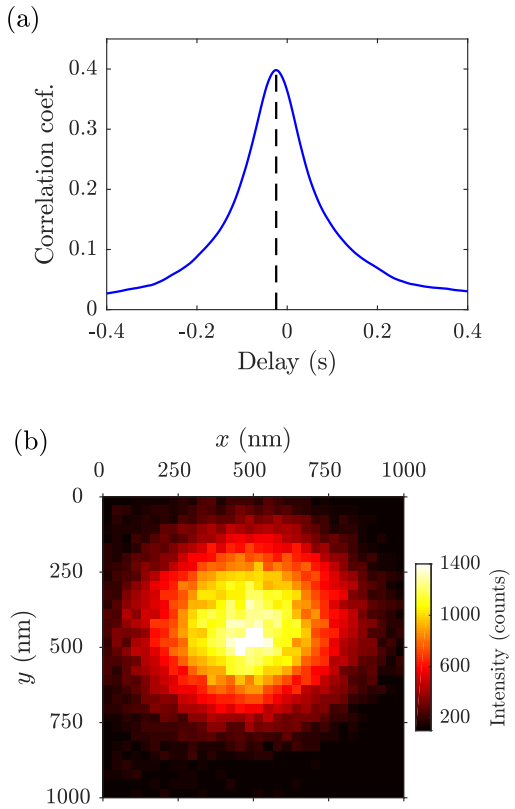

Fig. S2. (a) Correlation coefficient calculated from binary representations of the SPAD events and the camera detections. A dashed line represents the estimated time offset between the two channels. (b) Measured response of the SPAD while scanning a fluorescent bead in the sample plane.

In order to characterise the spatial correlation between SPAD events and camera detections, we must identify the pixels of the camera that are conjugated to the area of the sample seen by the SPAD. Hence, we measure the response of the SPAD by scanning a fluorescent bead with a diameter of 100 nm over a large area in the sample plane. Figure S2b shows the number of photons detected by the SPAD as a function of the bead position. The FWHM value of the measured profile is of the order of 500 nm, as expected from the diameter of the confocal pinhole (50 μm) and the magnification of the optical system ($\times$100). This response can be modelled by a function $h(x, y)$ which is the convolution of a 500 nm gate and a two-dimensional Gaussian function.

D. Association conditions

Once the time offset between the camera and the SPAD is estimated and compensated, we can quantify the time overlap between a camera detection and a SPAD event. To do so, we simply calculate the ratio of the time overlap Δt_{ij} to the time interval Δt_j corresponding to the SPAD event. The camera detection and the SPAD event are likely to be associated to the same molecule whenever this ratio is close to unity. We can then associate position and decay rate in the following situations:

- In 77% of the cases, the association between position and decay rate is straightforward. In such cases, only one camera detection is identified in the emission time Δt_j corresponding to a SPAD event. In addition, this SPAD event is the only one identified in the emission time Δt_i corresponding to the camera detection. Therefore, the camera detection i and the SPAD event j can be associated.

- In 18% of the cases, several camera detections at different positions are identified in Δt_j. In such cases, we can estimate the number of photons to be detected by the SPAD from a given camera detection. Let x_i and y_i be the coordinates in the sample plane corresponding to a detection and N_i the number of fluorescence photons measured by the camera, we can simply assume that the number of photons to be detected by the SPAD is proportional to $N_i\, h(x_i, y_i)$. An association condition can thus be set on the base of the value taken by $T_{ij} = N_i\, h(x_i, y_i)\Delta t_{ij}/\Delta t_j$. After the identification of the detection k on the camera associated with the maximum value of T_{ij}, we consider that the association between position and decay rate can be performed only if $T_{kj} > \alpha_a \sum_{i=1}^{n} T_{ij}$ where n is the number of camera detections in Δt_j and α_a is a threshold characterising the association condition. If α_a is low, camera detections are more frequently associated to SPAD events. However, this increases the number of cases in which the measured decay histograms are the sum of different decay histograms that cannot be properly separated by a post-processing analysis. As a trade-off, we use $\alpha_a = 80\%$ in the experiment.

- In 5% of the cases, several SPAD events are identified in Δt_i. Then, if the difference between these decay rates is smaller than 30%, we merge the SPAD events and we calculate the average decay rate. Otherwise, we evaluate the likelihood of each event to be the one corresponding to the camera detection, based on the number of fluorescence photons measured by the SPAD. To do so, we identify the event k associated with the highest number of photons N_k and we perform the association between position and decay rate only if $N_k > \alpha_a \sum_{i=1}^{n} N_i$ where N_i is the number of photons associated with the overlapping SPAD events and α_a is the threshold previously mentioned ($\alpha_a = 80\%$).

Post-process filtering Two additional conditions are required in order to correctly perform the association between position and decay rate. For each molecule, at least 150 fluorescence photons must be detected on each detector. Moreover, the standard deviation of the Gaussian function fitted to the camera data must be smaller than 190 nm. These two conditions avoid the occurrence of false detections that would be due to noise. Using this

procedure, we associate the position of 3,581 camera detections with their decay rate. We then perform post-processing filtering to account for the few remaining loopholes of the procedure. To do so, we compare each decay rate to the decay rate of the 10 closest detections. On average, this corresponds to a distance of 19 nm between the detection and its neighbours. Then, we perform an outlier identification based on the median absolute deviation (MAD). A decay rate Γ is rejected if the decay rates Γ_k of the closest neighbours satisfy the following condition:

$$|\Gamma - \mathrm{Med}(\Gamma_k)| > \alpha_r \ \mathrm{Med}\left[\frac{|\Gamma_k - \mathrm{Med}(\Gamma_k)|}{0.675}\right], \qquad \text{(S1)}$$

where Med is the median operator and α_r is a rejection threshold. The factor 0.675 is used so that MAD and standard deviation are approximately equal for large normal samples [8]. It should be noted that no outlier identification is performed if more than 50% of the neighbours have a decay rate equal to the upper limit previously mentioned (10 ns^{-1}) since the right-hand side of Eq. (S1) equals zero in this case. With the approach expressed by Eq. (S1), using a small threshold α_r allows the identification of many outliers but may also identify actual detections as outliers. As a trade-off, we use $\alpha_r = 5$ resulting in the identification of 6% of outliers. By removing them, the number of actual detections reduces to 3,352.

3. DENSITY AND INTENSITY MAPS

From data acquired by the EM-CCD camera, we can render a density map of the detected molecules (Fig. S3a), as for a usual single-molecule localisation-based super-resolution image reconstruction. In Fig. S3a, we observe strong density fluctuations due to an inhomogeneous labelling of our sample. However, note that for the purpose of obtaining a map of the LDOS, inhomogeneous labeling is not a limitation given a high enough spatial sampling, which underlines the robustness of our fluorescence lifetime measuring technique. It is important to underline that, in the image reconstruction in Fig. S3a, the strong density differences renders an image where black regions do not necessarily represent a lack of detections. In the case of biological applications, the labelling is specific to the protein of interest and thus density fluctuations represent structural changes of the sample which is not the case in our LDOS nanocartography.

Additionally, we can also reconstruct a color map coding the measured fluorescence intensity for each detection (Fig. S3b). Note that, if several molecules are detected within the same area, we plot the average intensity. While the density of detected molecules is higher along the sides of the nanowire than on the substrate, we observe that the collected intensity is lower for the molecules on the nanowire. Indeed, although the excitation field is larger for the molecules on the sides of the nanowire, their radiative quantum yield is reduced due to coupling to non-radiative modes (surface plasmon modes and quenching).

4. NUMERICAL SIMULATIONS

Simulations are performed using the FDTD simulation software MEEP [9]. The relative permittivity of silver is modelled with a Lorentz–Drude model, the relative permittivity of the buffer solution is set to 1.77 and the relative permittivity of glass is set to 2.25. In order to estimate the influence of the excitation field on the observed density variations, we model the system in two dimensions, with a mesh resolution of 0.5 nm. The nanowire, located on a glass substrate, is illuminated by a plane wave at

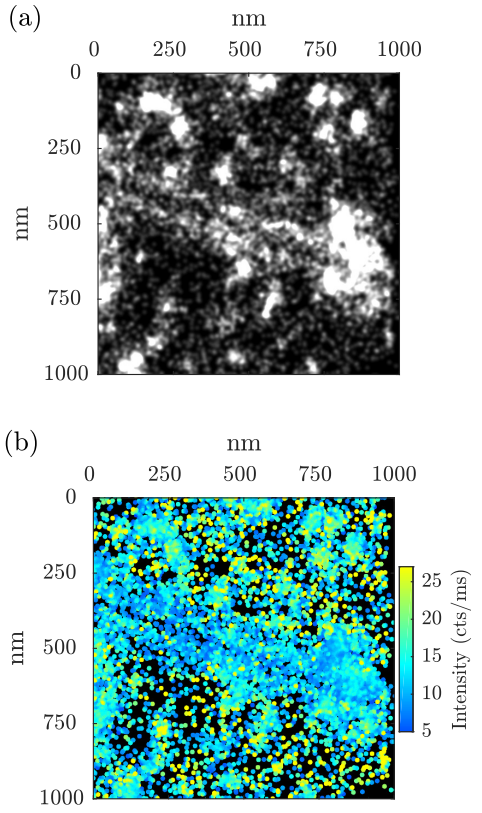

Fig. S3. (a) Density and (b) intensity maps reconstructed from the 14,546 molecules detected by the EM-CCD camera.

$\lambda = 640$ nm polarised perpendicularly to the nanowire, as in the experiment. In this configuration, a two-dimensional simulation gives the exact solution due to the invariance of the structure and the source along the longitudinal dimension. In contrast, in order to study the decay rate enhancement due to the nanowire, we model the system in three dimensions, with a mesh resolution of 1 nm. As the effect of the substrate on the decay rate is small due to the low contrast between the relative permittivities of the buffer solution and the glass coverslip, we perform the simulations without the substrate to limit the computational time. In each simulation, the emitter is modelled as an electric dipole source that generates a Gaussian pulse at $\lambda = 670$ nm, and the decay rate is estimated from the value of the electric field at the source position. We assume that the intrinsic quantum yield of Alexa Fluor 647 dyes is 0.33, as specified by the provider, in order to calculate the total decay rate enhancement.

5. DECAY HISTOGRAMS OF SINGLE MOLECULES

In this section, we show decay histograms for different molecules far from the nanowire and in its close vicinity, providing clear evidence of the decay rate enhancement. Figure S4 (a) to (f) shows the signal measured by the camera and by the SPAD during the experiment for three molecules characterised by different decay rate. Figure S4 (g) shows the associated decay histograms, together with mono-exponential fits. While the decay rate of the molecule far from the nanowire is not enhanced (molecule 1), the decay rate of the two molecules in the close vicinity of the nanowire show a strong decay rate enhancement (molecules 2 and 3). For the third molecule considered, the decay

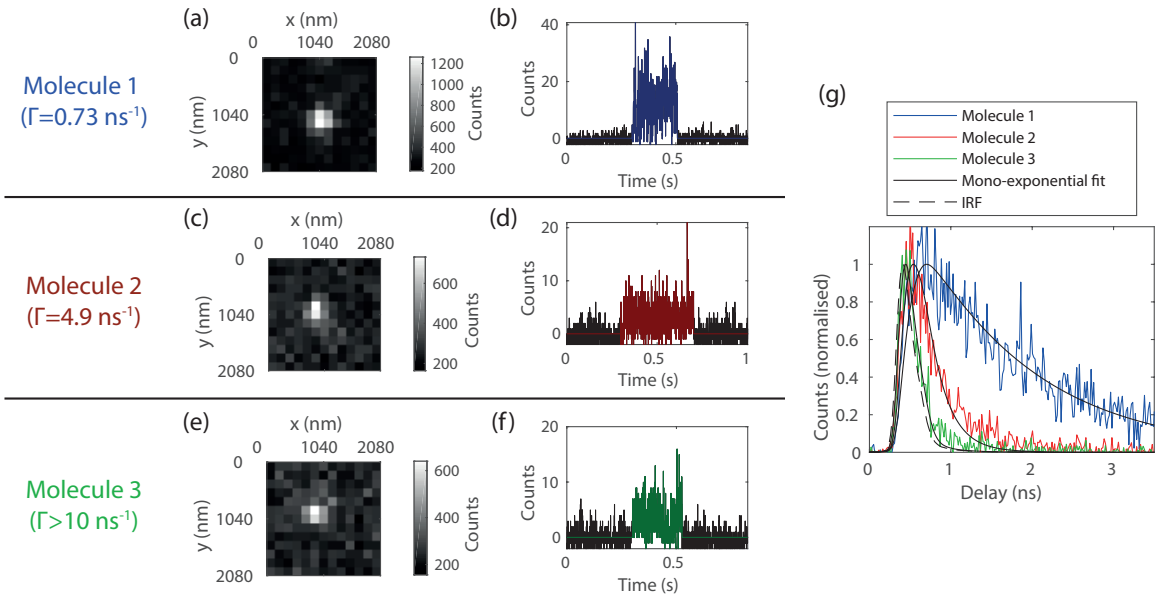

Fig. S4. Camera images and signal measured by the SPAD for a molecule far from the nanowire [sub-figures (a) and (b)], for a molecule close to the nanowire with $\Gamma/\Gamma_0 \sim 7$ [sub-figures (c) and (d)], and for a molecule close to the nanowire with $\Gamma/\Gamma_0 > 15$ [sub-figures (e) and (f)]. The associated decay histograms are shown in sub-figure (g).

rate cannot be resolved by the current experimental setup as the decay histogram and the IRF are superimposed.

6. CRAMÉR-RAO ANALYSIS: POSITION ESTIMATIONS

To estimate the Cramér-Rao lower bound on the standard error of position estimators $\sigma_{\bar{x},\bar{y}}$, we follow the approach described in [10]. The data acquired by the EM-CCD camera are modeled using the Airy function to describe the fluorescence signal, as well as a uniform background noise originating from the luminescence of the substrate. Then, we consider that the probability density function describing the number of photoelectrons per pixel is given by the convolution of the amplified signal and the Gaussian readout noise. The information matrix is calculated from this probability density function, and numerically inverted in order to compute the Cramér-Rao bound.

Point spread function We consider the simple situation in which a far-field microscope is used to collect the photons emitted by a single molecule located in the object plane. We assume that the 2-dimensional probability density function (PDF) describing the intensity distribution in the image plane can be expressed from the coordinates in the image plane noted (x', y') and the coordinates of the molecule in the object plane noted (x_0, y_0) as follows:

$$q(x', y') = \frac{J_1^2\left(\dfrac{2\pi \mathrm{NA}\sqrt{(x'-Mx_0)^2+(y'-My_0)^2}}{M\lambda_0}\right)}{\pi\left[(x'-Mx_0)^2+(y'-My_0)^2\right]}, \quad \text{(S2)}$$

where J_1 is the first-order Bessel function of the first kind, NA is the numerical aperture of the objective, M is the magnification and λ_0 is the free-space emission wavelength. The expectation of each data item – that is, the expectation of the value measured on each pixel by the camera – is then expressed as follows:

$$\begin{aligned} f_i = & N \int_{(x',y')\in pixel} q(x', y')\,\mathrm{d}x'\,\mathrm{d}y' \\ & + N_b \int_{(x',y')\in pixel} q_b(x', y')\,\mathrm{d}x'\,\mathrm{d}y' , \end{aligned} \quad \text{(S3)}$$

where N is the total number of photons emitted by the molecule and detected by the camera and N_b is the number of photons due to background noise which follows a PDF noted $q_b(x', y')$. In Eq. (S3), the integration is performed over the area that defines the considered pixel. Note that a dedicated study of the point spread function in our geometry could improve the prediction of position of the dipoles along the nanowire [11].

EM-CCD data model We can now derive a functional form for the likelihood function that describes the number of events measured on each pixel by the camera. Assuming that fluorescence photons detected by the camera are statistically independent, the number of photons impinging on each pixel during a given time interval follows a Poisson distribution of expectation f_i. If we do not consider the additional noise arising from the detection process, the PDF associated with the observation of X photoelectrons on a given pixel is

$$p_i^p(X;\boldsymbol{\theta}) = \frac{f_i^X}{X!}\, e^{-f_i} , \quad \text{(S4)}$$

where $\boldsymbol{\theta}$ are the parameters that must be estimated from the data (here, the parameters are the coordinates of the molecule). This sets the fundamental limit achievable by a perfect camera. However, the multiplication register of an EM-CCD camera enhances the number of generated photoelectrons in order to beat the readout noise of the camera, and the PDF followed by the number of photoelectrons generated by the process depends

on the gain g. As shown in Ref. [12], this PDF noted $p_i^e(X;\boldsymbol{\theta})$ can be approximated, for large gain values, by

$$p_i^e(X;\boldsymbol{\theta}) = \begin{cases} e^{-f_i}, & \text{for } X = 0\,, \\ \dfrac{e^{(-X/g-f_i)}\sqrt{\dfrac{f_i X}{g}}\, I_1\left(2\sqrt{\dfrac{f_i X}{g}}\right)}{X}, & \text{for } X > 0\,, \end{cases} \tag{S5}$$

where I_1 is the first-order modified Bessel function of the first kind. In addition, the readout process induces a Gaussian noise on each pixel characterised by an expectation η_g and a standard deviation σ_g. This Gaussian noise can be described by the following PDF:

$$p^g(X;\boldsymbol{\theta}) = \frac{1}{\sigma_g\sqrt{2\pi}} \exp\left(-\frac{(X-\eta_g)^2}{2\sigma_g^2}\right)\,. \tag{S6}$$

The PDF describing the readout noise of the camera is the same for all the pixels. Therefore, we can consider that the PDF describing the number of photoelectrons per pixel for a real EMCCD camera is given by

$$p_i(X;\boldsymbol{\theta}) = \left[p_i^e(X;\boldsymbol{\theta})\right] * \left[p^g(X;\boldsymbol{\theta})\right]\,, \tag{S7}$$

where the asterisk ($*$) represents the convolution product. Then, the information matrix can be numerically evaluated from its general expression given by [13]

$$\left[\mathcal{I}(\boldsymbol{\theta})\right]_{jk} = \sum_{i=1}^{n} \mathrm{E}\left[\frac{1}{\left[p_i(X;\boldsymbol{\theta})\right]^2}\left(\frac{\partial p_i(X;\boldsymbol{\theta})}{\partial\theta_j}\right)\left(\frac{\partial p_i(X;\boldsymbol{\theta})}{\partial\theta_k}\right)\right]\,. \tag{S8}$$

Cramér-Rao bound After having experimentally measured the value of the parameters involved in the model, we can compute the Cramér-Rao bound on the variance of position estimators in order to evaluate a lower bound on the standard error $\sigma_{x,y}$ on the position estimates performed using one frame. Assuming that there is no preferred direction in space – this is not exactly true because of the shape of the pixels, but is a good approximation for squared pixels – the Cramér-Rao inequality reads

$$\sigma_{x,y} \geq \sqrt{\frac{1}{\mathcal{I}_{xx}}} = \sqrt{\frac{1}{\mathcal{I}_{yy}}}\,. \tag{S9}$$

In the experiment, a molecule is typically detected on two successive frames. Its position is then estimated by the mean of the individual estimates, so that the standard error on the resulting position estimate is $\sigma_{\bar{x},\bar{y}} = \sigma_{x,y}/\sqrt{2}$. Different situations can then be compared: the fundamental is calculated using Eq. (S4) with $N_b = 0$, the instrumental limit is calculated using Eq. (S7) with $N_b = 0$, and the experimental limit is calculated using Eq. (S7) with the value of N_b measured in the experiment.

7. CRAMÉR-RAO ANALYSIS: DECAY RATE ESTIMATIONS

To estimate the Cramér-Rao lower bound on the relative standard error of decay rate estimators σ_Γ/Γ, we adopt a similar approach, described in [14]. In order to estimate the Cramér-Rao bound for our experiment, we model the fluorescence decay by the convolution of the IRF and an exponential distribution. After proper inclusion of time-dependent background noise in the model, it can then be considered that each point of the decay histogram follows a Poisson distribution. Thus, we can compute the information matrix from this distribution and numerically invert it in order to obtain the Cramér-Rao bound.

SPAD data model By modelling a molecule by a two-level system, the PDF that describes the photon emission time t is given by an exponential distribution. Since the agreement between experimental data and the mono-exponential model is satisfactory, we consider here that this model is relevant. Then, the PDF followed by the photon detection time measured by the experimental system is

$$q(t) = q_{irf}(t) * \left[\Gamma e^{-\Gamma t}\right]\,, \tag{S10}$$

where $q_{irf}(t)$ is the PDF describing the IRF of the setup. From this expression, we can find the expectation of each data item; that is, the expectation of each data point of the decay histogram. We obtain

$$f_i = N\sum_{l=0}^{+\infty}\int_{t_i+lT}^{t_{i+1}+lT} q(t)\,\mathrm{d}\,t + N_b\int_{t_i}^{t_{i+1}} q_b(t)\,\mathrm{d}\,t\,, \tag{S11}$$

where N is the number of photons emitted by the molecule and detected by the system, N_b is the number of detected photons due to background noise which follows a PDF noted $q_b(t)$, and T is the repetition period of the laser. If the fluorescence lifetime of the molecule is much smaller than the repetition period, only the first term of the sum in Eq. (S11) is significant.

In general, SPADs have negligible readout noise and the dark count rate contributes to the background noise. Thus, we can model the distribution of photons detected for each data point by a Poisson distribution of expectation f_i. The PDF associated with the observation of X events on a given data point is then expressed by

$$p_i(X;\boldsymbol{\theta}) = \frac{f_i^X}{X!}e^{-f_i}\,. \tag{S12}$$

The set of parameters that must be estimated from the data is $\boldsymbol{\theta} = (N,\Gamma)$, while we estimate $q_{irf}(t)$, $q_b(t)$ and N_b with independent measurements. Then, the information matrix can be calculated from Eq. (S8).

Cramér-Rao bound After having experimentally measured the value of the parameters involved in the model, we can compute the Cramér-Rao bound on the standard error σ_Γ on the decay rate estimates. The Cramér-Rao inequality can be expressed as

$$\frac{\sigma_\Gamma}{\Gamma} \geq \frac{1}{\sqrt{N}} \times F\left(T, N_b, q_{irf}, q_b, n\right)\,, \tag{S13}$$

where n is the number of data points and F is calculated by numerically inverting the information matrix [14].

REFERENCES

1. L. Lermusiaux, V. Maillard, and S. Bidault, "Widefield Spectral Monitoring of Nanometer Distance Changes in DNA-Templated Plasmon Rulers," ACS Nano **9**, 978–990 (2015).
2. M. Heilemann, S. van de Linde, M. Schüttpelz, R. Kasper, B. Seefeldt, A. Mukherjee, P. Tinnefeld, and M. Sauer, "Subdiffraction-Resolution Fluorescence Imaging with Conventional Fluorescent Probes," Angewandte Chemie Int. Ed. **33**, 6172–6176 (2008).
3. S. van de Linde, A. Löschberger, T. Klein, M. Heidbreder, S. Wolter, M. Heilemann, and M. Sauer, "Direct stochastic optical reconstruction microscopy with standard fluorescent probes," Nat. Protoc. **6**, 991–1009 (2011).

4. A. Gulinatti, I. Rech, F. Panzeri, C. Cammi, P. Maccagnani, M. Ghioni, and S. Cova, "New silicon SPAD technology for enhanced red-sensitivity, high-resolution timing and system integration," J. Mod. Opt. **59**, 1489–1499 (2012).
5. C. A. Schneider, W. S. Rasband, and K. W. Eliceiri, "NIH Image to ImageJ: 25 years of image analysis," Nat. Methods **9**, 671 (2012).
6. M. Ovesný, P. Křížek, J. Borkovec, Z. Švindrych, and G. M. Hagen, "ThunderSTORM: a comprehensive ImageJ plug-in for PALM and STORM data analysis and super-resolution imaging," Bioinformatics **30**, 2389–2390 (2014).
7. I. Izeddin, J. Boulanger, V. Racine, C. G. Specht, A. Kechkar, D. Nair, A. Triller, D. Choquet, M. Dahan, and J. B. Sibarita, "Wavelet analysis for single molecule localization microscopy," Opt. Express **20**, 2081–2095 (2012).
8. R. A. Maronna, D. R. Martin, and V. J. Yohai, "Dispersion estimates," in *Robust Statistics: Theory and Methods*, (Wiley-Blackwell, Chichester, 2006), pp. 32–34.
9. A. F. Oskooi, D. Roundy, M. Ibanescu, P. Bermel, J. D. Joannopoulos, and S. G. Johnson, "Meep: A flexible free-software package for electromagnetic simulations by the FDTD method," Comput. Phys. Commun. **181**, 687–702 (2010).
10. J. Chao, E. S. Ward, and R. J. Ober, "Fisher information theory for parameter estimation in single molecule microscopy: tutorial," JOSA A **33**, B36–B57 (2016).
11. L. Su, G. Lu, B. Kenens, S. Rocha, E. Fron, H. Yuan, C. Chen, P. Van Dorpe, M. B. J. Roeffaers, H. Mizuno, J. Hofkens, J. A. Hutchison, and H. Uji-i, "Visualization of molecular fluorescence point spread functions via remote excitation switching fluorescence microscopy," Nat. Commun. **6**, 7287 (2015).
12. J. Chao, E. S. Ward, and R. J. Ober, "Fisher information matrix for branching processes with application to electron-multiplying charge-coupled devices," Multidimens. systems signal processing **23**, 349–379 (2012).
13. S. Kay, *Fundamentals of Statistical Processing, Volume I: Estimation Theory* (Prentice Hall, Englewood Cliffs, N.J, 1993).
14. D. Bouchet, V. Krachmalnicoff, and I. Izeddin, "Fisher information theory for optimised lifetime estimations in time-resolved fluorescence microscopy," arXiv:1809.04149 [physics] (2018).